

8-2017

Nanostructure Evolution of Magnetron Sputtered Hydrogenated Silicon Thin Films

Dipendra Adhikari

Maxwell M. Junda

Sylvain X. Marsillac
Old Dominion University

Robert W. Collins

Nikolas J. Podraza

Follow this and additional works at: https://digitalcommons.odu.edu/ece_fac_pubs

 Part of the [Electrical and Electronics Commons](#), [Electronic Devices and Semiconductor Manufacturing Commons](#), and the [Engineering Physics Commons](#)

Repository Citation

Adhikari, Dipendra; Junda, Maxwell M.; Marsillac, Sylvain X.; Collins, Robert W.; and Podraza, Nikolas J., "Nanostructure Evolution of Magnetron Sputtered Hydrogenated Silicon Thin Films" (2017). *Electrical & Computer Engineering Faculty Publications*. 136.
https://digitalcommons.odu.edu/ece_fac_pubs/136

Original Publication Citation

Adhikari, D., Junda, M. M., Marsillac, S. X., Collins, R. W., & Podraza, N. J. (2017). Nanostructure evolution of magnetron sputtered hydrogenated silicon thin films. *Journal of Applied Physics*, 122, 075302. doi:10.1063/1.4998455

Nanostructure evolution of magnetron sputtered hydrogenated silicon thin films

Dipendra Adhikari, Maxwell M. Junda, Sylvain X. Marsillac, Robert W. Collins, and Nikolas J. Podraza

Citation: *Journal of Applied Physics* **122**, 075302 (2017); doi: 10.1063/1.4998455

View online: <http://dx.doi.org/10.1063/1.4998455>

View Table of Contents: <http://aip.scitation.org/toc/jap/122/7>

Published by the [American Institute of Physics](#)

Articles you may be interested in

[The stochastic growth of metal whiskers](#)

Applied Physics Letters **110**, 251604 (2017); 10.1063/1.4989852

[Structural and spectroscopic analysis of ex-situ annealed RF sputtered aluminium doped zinc oxide thin films](#)

Journal of Applied Physics **122**, 075303 (2017); 10.1063/1.4998939

[Physical properties of nanometer graphene oxide films partially and fully reduced by annealing in ultra-high vacuum](#)

Journal of Applied Physics **122**, 075301 (2017); 10.1063/1.4998812

[Temperature-dependent activation energy of electromigration in Cu/porous low-k interconnects](#)

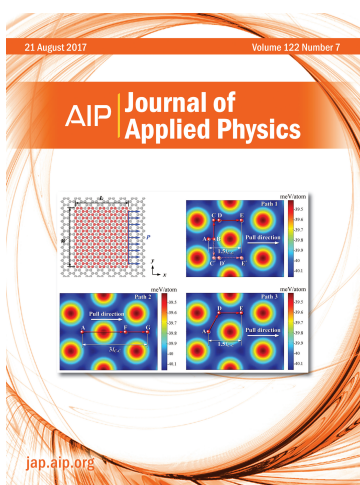
Journal of Applied Physics **122**, 074501 (2017); 10.1063/1.4998523

[Structure and photoluminescence study of silicon based two-dimensional Si₂Te₃ nanostructures](#)

Journal of Applied Physics **122**, 075701 (2017); 10.1063/1.4998811

[Size effect on interlayer shear between graphene sheets](#)

Journal of Applied Physics **122**, 074301 (2017); 10.1063/1.4997607



Nanostructure evolution of magnetron sputtered hydrogenated silicon thin films

Dipendra Adhikari,¹ Maxwell M. Junda,¹ Sylvain X. Marsillac,² Robert W. Collins,¹ and Nikolas J. Podraza¹

¹*Department of Physics and Astronomy and The Wright Center for Photovoltaics Innovation and Commercialization, University of Toledo, Toledo, Ohio 43606, USA*

²*Virginia Institute of Photovoltaics, Old Dominion University, Norfolk, Virginia 23529, USA*

(Received 10 April 2017; accepted 31 July 2017; published online 17 August 2017)

Hydrogenated silicon (Si:H) thin films have been prepared by radio frequency (RF) magnetron sputtering. The effect of hydrogen gas concentration during sputtering on the resultant film structural and optical properties has been investigated by real time spectroscopic ellipsometry (RTSE) and grazing incidence x-ray diffraction (GIXRD). The analysis of *in-situ* RTSE data collected during sputter deposition tracks the evolution of surface roughness and film bulk layer thickness with time. Growth evolution diagrams depicting amorphous, nanocrystalline, and mixed-phase regions for low and high deposition rate Si:H are constructed and the effects of process parameter (hydrogen gas concentration, total pressure, and RF power) variations on the deposition rate have been qualified. Virtual interface analysis of RTSE data provides nanocrystalline volume fraction depth profiles in the mixed-phase growth regime. GIXRD measurements show the presence of (111) and (220) oriented crystallites. Vibrational mode absorption features from Si-H_n bonding configurations at 590, 640, 2000, and 2090 cm⁻¹ are obtained by *ex-situ* infrared spectroscopic ellipsometry. Hydrogen incorporation decreases as films transition from amorphous to nanocrystalline phases with increasing hydrogen gas concentration during sputtering. *Published by AIP Publishing.* [<http://dx.doi.org/10.1063/1.4998455>]

I. INTRODUCTION

Hydrogenated amorphous silicon (a-Si:H) and hydrogenated nanocrystalline silicon (nc-Si:H) are used in solar cells largely as a result of the Earth's abundance of Si and cost effective, scalable deposition techniques. Both a-Si:H and nc-Si:H are useful in single or multi-junction thin film photovoltaics (PV), while a-Si:H is also used as a passivation layer in single- or multi-crystalline Si heterojunction ("HIT") cells.^{1,2} Incorporation of hydrogen into the a-Si matrix and at crystallite grain boundaries passivates dangling bonds and defect states to enhance the optoelectronic properties of the material and final device.^{3,4} Thin film Si:H can be deposited using a variety of techniques including radio frequency (RF) plasma enhanced chemical vapor deposition (PECVD), very high frequency (VHF) PECVD, hot-wire gas dissociation, and others. The literature describing some of these techniques, PECVD in particular, is extensive.^{1,5-13} In this study, we deposit thin Si:H films using RF magnetron sputtering of an undoped Si target in a mixed argon and hydrogen (Ar + H₂) gas ambient atmosphere. Although existing literature describing RF-sputtered thin film Si is comparatively less comprehensive than that describing other deposition techniques, sputtering potentially offers significant advantages.¹⁴⁻¹⁶ Sputtering provides the opportunity to avoid the use of hazardous precursor gases (i.e., SiH₄, Si₂H₆) associated with PECVD and other gas-phase dissociation techniques while maintaining effective control over many microstructural properties of the resultant films including crystallinity, hydrogen incorporation, and surface morphology, all of which are of interest in the various applications of thin Si:H films.

The goal of this study is to investigate the phase evolution of sputtered Si:H films and to produce a-Si:H and nc-Si:H materials at reasonable deposition rates, > 1 Å/s, for possible future evaluation in PV devices. We employ *in-situ*, real time spectroscopic ellipsometry (RTSE) measurements of the growing film to non-destructively characterize optical properties and evolution of nanostructure in the material during deposition.¹⁷ Moreover, RTSE is especially useful when the material grows with structural inhomogeneity such as crystallite nucleation from an amorphous matrix. Here, we use RTSE to track the influence of H₂ partial pressure or gas concentration on the amorphous roughening [(a → a)], amorphous to mixed-phase amorphous + nanocrystalline [a → (a + nc)], and mixed-phase to single-phase nanocrystalline [(a + nc) → nc] structural transitions. Although these transitions occurring during PECVD of thin film Si:H are already well characterized,⁵⁻¹⁰ RF sputtered Si:H has not received the same attention and comparatively less is known about its microstructural growth processes.

Ex-situ Raman spectroscopy and x-ray diffraction (XRD) measurements are commonly used experimental techniques to investigate the crystalline volume fraction in the material. These techniques differ from RTSE in that the XRD measurement averages information over the full depth of a thin film sample, whereas Raman spectroscopy averages information from a limited depth of the sample. In some cases, *ex-situ* Raman spectroscopy may yield a significantly different result compared to XRD measurement.¹⁸ Presently, there has been growing interest in *in-situ* measurement including spectroscopic ellipsometry⁵⁻¹⁰ and Raman spectroscopy¹⁹ to track

the variation in crystallinity as a function of depth throughout a full film. Complementary microstructural properties of Si:H films, relative to those from *in-situ* RTSE, have been studied using XRD,^{11,15,20,21} which reveals several peaks corresponding to different Si crystallite orientations.

We have performed grazing incidence x-ray diffraction (GIXRD) measurements of Si:H films fabricated under varying conditions to correlate crystallographic properties with RTSE results. In previous studies, infrared (IR) spectroscopy^{11,20–34} has been used to investigate the Si-H_n bonding configurations in Si:H. Observation shows that Si:H may contain several IR absorption features including stretching modes at 2000, 2090, and 2120 cm⁻¹; bending modes at 850 and 890 cm⁻¹; and wagging or rocking modes at 640 and 590 cm⁻¹, respectively, with the distribution of these modes often depending on the method of fabrication.^{22,35} IR spectroscopic ellipsometry is used in this study, providing a method for identifying these IR vibrational modes in each film and inferring relative information about interrelationships between hydrogen incorporation and nanostructure when compared to RTSE and XRD results.

II. EXPERIMENTAL DETAILS

Si:H films have been deposited onto native oxide coated single crystal Si wafer substrates at 200 °C using RF (13.56 MHz) magnetron sputtering of a 3-in. diameter undoped Si target with a target-to-substrate separation of 13.5 cm. The H₂ to total gas flow ratio ($p_{\text{H}_2} = [\text{H}_2]/([\text{H}_2] + [\text{Ar}]) \times 100\%$) is maintained constant during each deposition. Two series of Si:H films have been deposited, one under conditions yielding a low deposition rate (~ 0.15 Å/s) and another with conditions resulting in a higher deposition rate (~ 1.3 Å/s). In each series, p_{H_2} was varied. The low rate series has been deposited at a total gas pressure $p_{\text{tot}} = 30$ mTorr and RF power = 100 W and the high rate films at $p_{\text{tot}} = 10$ mTorr and RF power = 250 W.

In-situ RTSE measurements are performed using a dual rotating compensator multichannel ellipsometer (Model RC2-XI, J. A. Woollam Co., Inc.)³⁶ over the near infrared to ultraviolet spectral range of 0.74–5.90 eV at 70° angle of incidence. Real time ellipsometric spectra are collected at 4.18 s intervals during deposition. IR-range ellipsometric spectra are collected *ex-situ* by a Fourier transform, rotating compensator IR ellipsometer (Model IR-VASE, J. A. Woollam Co., Inc.)³⁷ over a spectral range of 0.05–0.62 eV (400–5000 cm⁻¹). As has been demonstrated previously for PECVD Si:H, the optical response in the form of the spectra in the complex dielectric function, $\varepsilon = \varepsilon_1 + i\varepsilon_2$, and microstructural properties are extracted using a global $\sum \sigma(t)$ -minimization procedure with an unweighted error function.⁶ An optical model consisting of ambient/surface roughness/bulk thin film Si:H/interfacial layer/native oxide/semi-infinite single crystal Si is used to fit both RTSE and FTIR-extended measurements. The optical responses of the surface roughness and interfacial layer are described by a Bruggeman effective medium approximation (EMA)^{38,39} consisting of two material components with optical properties ε_{mat} and $\varepsilon_{\text{void}}$, and defined by

$$\left(\frac{\varepsilon_{\text{mat}} - \varepsilon}{\varepsilon_{\text{mat}} + 2\varepsilon} \right) f_{\text{mat}} + \left(\frac{\varepsilon_{\text{void}} - \varepsilon}{\varepsilon_{\text{void}} + 2\varepsilon} \right) f_{\text{void}} = 0, \quad (1)$$

where f_{mat} and f_{void} are the volume fractions of the material and void, respectively, each fixed at 0.5 here. Each individual measurement has 1067 complex (ψ , Δ) pairs at different photon energies, and in order to extract a common set of spectra in ε for the early stages of film growth, 5 sets of spectroscopic measurements, selected from among those acquired before any $a \rightarrow (a + nc)$ transitions are observed, are analyzed simultaneously. The structural parameters consist of bulk and surface roughness layer thicknesses for each experimental set of spectra along with an additional nucleation layer thickness fit to a common value for all 5 sets of spectra in the analysis. Values of ε are deduced at each photon energy. This type of procedure is described in Refs. 5–10, 12, 13, 38, 40, and 41. The surface roughness thickness can vary significantly over the deposition, depending on the structural evolution. A void-rich interfacial or nucleation layer has been previously observed in the early stages of growth for a-Si:H⁷ and nc-Si:H.⁴² The interfacial layer thickness ranges from 0 to 54.1 ± 0.4 Å for all films studied here, and remains static once a bulk film layer develops. GIXRD measurements are performed with a Rigaku/Altima-III X-ray diffractometer using Cu-K α radiation ($\lambda = 1.54059$ Å) and provide complementary information about the overall crystallographic structure.

III. RESULTS AND DISCUSSION

A. Growth evolution diagrams

As has been observed for PECVD Si:H,^{5,6,12} RF sputtered Si:H films can exhibit structural transitions at different thicknesses during deposition. In particular, we identify the thicknesses of $a \rightarrow (a + nc)$ and $(a + nc) \rightarrow nc$ structural transitions corresponding to the nucleation of crystallites from the amorphous phase [$a \rightarrow (a + nc)$] followed by their coalescence [$(a + nc) \rightarrow nc$], as well as the $a \rightarrow a$ roughening transition corresponding to a transition from a stable surface with unchanging roughness to a surface that is continuously roughening within the amorphous growth regime. These structural transitions can be identified directly from their effects on the surface roughness thickness (d_s) and from spectra in ε as a function of bulk film thickness (d_b) during Si:H growth, as obtained by fitting RTSE measurements as previously described. Optically determined surface roughness has been previously shown to correlate with values obtained by atomic force microscopy.³⁸ Figure 1 shows examples of d_s evolution as a function of d_b for two different films fabricated at a low deposition rate. The film prepared at $p_{\text{H}_2} = 20\%$ undergoes characteristic $a \rightarrow (a + nc)$ and $(a + nc) \rightarrow nc$ transitions at d_b , corresponding to the abrupt increase in d_s , and at the maximum in d_s , respectively. By contrast, the film prepared at $p_{\text{H}_2} = 15\%$ features a smooth stable surface which is followed by slight roughening dictated by atomic scale self-shadowing involved in the $a \rightarrow a$ transition.^{13,43} Both $a \rightarrow a$ and $a \rightarrow (a + nc)$ transition thicknesses are identified as the d_b value at 1 Å increase in d_s above the minimum d_s thickness; however, the $a \rightarrow (a + nc)$ transition is differentiated from the

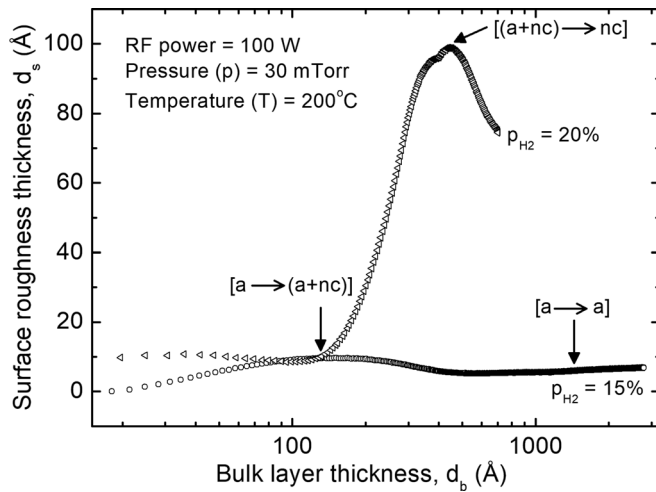


FIG. 1. Variation of the surface roughness thickness (d_s) with bulk layer thickness (d_b) obtained from analysis of real time spectroscopic ellipsometry (RTSE) data collected for two Si:H films prepared at RF power = 100 W and total gas pressure = 30 mTorr with relative hydrogen gas concentrations $p_{H_2} = [H_2]/([H_2] + [Ar]) \times 100\% = 15\%$ and 20%.

$a \rightarrow a$ transition in that the quality of fit is significantly poorer in the mixed phase regime as a result of the continued use of optical properties describing only a-Si:H and not an (a + nc)-Si:H mixture.

Figure 2 shows the growth evolution diagrams of sputtered Si:H prepared at a substrate temperature of 200 °C for both low and high deposition rates. The $a \rightarrow a$, $a \rightarrow (a + nc)$, and $(a + nc) \rightarrow nc$ structural transitions observed in Fig. 2 are qualitatively similar to those observed in PECVD Si:H.⁶ The films remain amorphous at low values of p_{H_2} , whereas nanocrystallites nucleate from the amorphous phase at relatively moderate to high p_{H_2} . In the case of both the film series, the thicknesses corresponding to the $a \rightarrow (a + nc)$ and $(a + nc) \rightarrow nc$ transitions shift to a lower bulk film thickness with increasing p_{H_2} , demonstrating that higher hydrogen gas concentrations create more favorable conditions for nanocrystallite nucleation and growth. These trends are qualitatively similar to those observed in PECVD, where crystallite nucleation begins to occur at certain hydrogen-to-silicon-carrying-gas flow ratios and the thickness at which these transitions appear shifts to lower thicknesses with increased hydrogen present.

A virtual interface analysis (VIA)^{7,8} is applied to RTSE data to extract a depth profile of the nanocrystallite volume fraction in the mixed-phase regime. This is accomplished by treating the outermost ~ 50 Å of material as a discrete layer described by a Bruggeman EMA consisting of variable fractions of a-Si:H and nc-Si:H. Spectra in ϵ describing a-Si:H are obtained from fitting to RTSE measurements at $d_b \approx 200$ Å, i.e., before nanocrystallite nucleation. The optical properties that best represent the nc-Si:H in the spectral range from 2.5 to 5 eV are obtained by fitting to RTSE measurements at the end of the deposition where the film has transformed to a single phase nanocrystalline material using the multi-step procedure described in Ref. 9. The procedure begins by setting a trial value for the roughness layer thickness, generating the optical properties of the pseudo-substrate, and using it as a semi-infinite substrate with a nc-

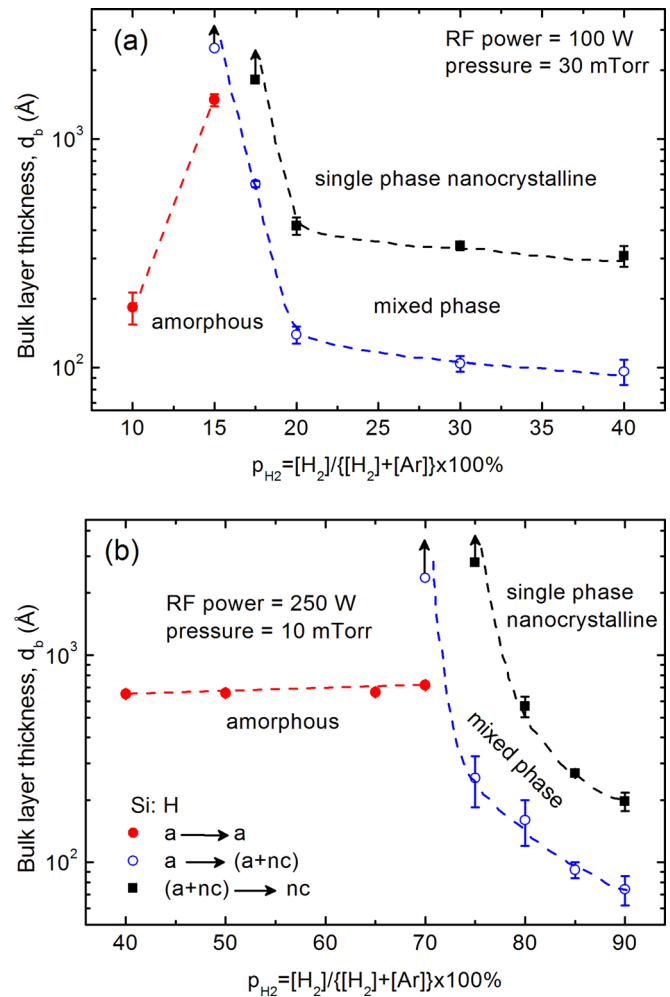


FIG. 2. Growth evolution diagrams of Si:H obtained from RTSE depicting thicknesses at which the amorphous-to-amorphous roughening [$a \rightarrow a$] (solid circles), amorphous to mixed-phase amorphous + nanocrystalline [$a \rightarrow (a + nc)$] (open circles), and mixed-phase to single-phase nanocrystalline [$(a + nc) \rightarrow nc$] (solid squares) transitions occur for films prepared at (a) low and (b) high deposition rates as a function of p_{H_2} . The upward arrows indicate that the associated transition had not yet been reached at the maximum accumulated thickness of the film measured. The dashed lines are included as rough guides to the eye representing approximate boundaries between two regimes.

Si:H bulk over layer and surface roughness. This step is repeated for various reasonable values of surface roughness thicknesses to extract spectra in ϵ of the nc-Si:H bulk layer. Finally, the extracted optical properties of the bulk layer are used in a three component EMA (a-Si:H, nc-Si:H, and void) along with the $\sum \sigma$ -minimization approach within VIA to obtain the lowest error in the fitting for the mixed-phase regime. This minimum error identifies the correct surface roughness thickness and from it the most realistic optical properties of nc-Si:H. Figure 3 depicts a comparison of a-Si:H and nc-Si:H reference spectra in ϵ for a high deposition rate film with $p_{H_2} = 80\%$, used within VIA of RTSE data. The optical response of nc-Si:H is characterized by the presence of two critical point features reminiscent of single crystal Si while a-Si:H has only one broad feature.⁹ The depth profile of the nanocrystallite fraction (f_{nc}) in the mixed-phase regime obtained from a representative VIA of a high deposition rate film with $p_{H_2} = 80\%$ is shown in Fig. 4. The correspondence between the evolution of both d_s and f_{nc} seen in

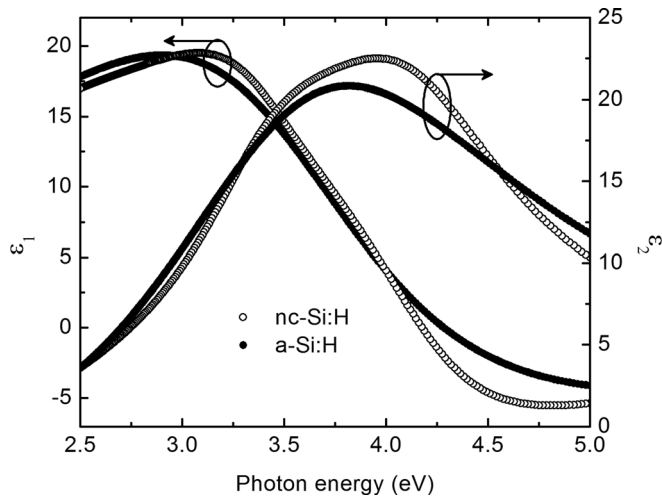


FIG. 3. Complex dielectric function, $\epsilon = \epsilon_1 + i\epsilon_2$, spectra for a-Si:H and nc-Si:H used as reference optical properties in the virtual interface analysis (VIA). Spectra in ϵ for a-Si:H and nc-Si:H are obtained at different thicknesses from the film produced at RF power = 250 W, $p_{\text{tot}} = 10$ mTorr, and $p_{\text{H}_2} = 80\%$.

Fig. 4 provides justification for the previously described technique of using d_s as a function of d_b to identify phase transition thicknesses as has also been applied previously for PECVD Si:H materials.

B. Deposition rates

Deposition rates are determined from the analysis of RTSE data using ϵ obtained from fitting to measurements corresponding to $d_b \approx 200$ Å. A linear relationship is used to fit d_b as a function of deposition time, with the slope yielding the deposition rate of each sample studied. Figure 5 depicts the rates of deposition of Si:H samples for the low and high deposition rate series as functions of p_{H_2} . In general, increasing pressure typically decreases sputter deposition rates by

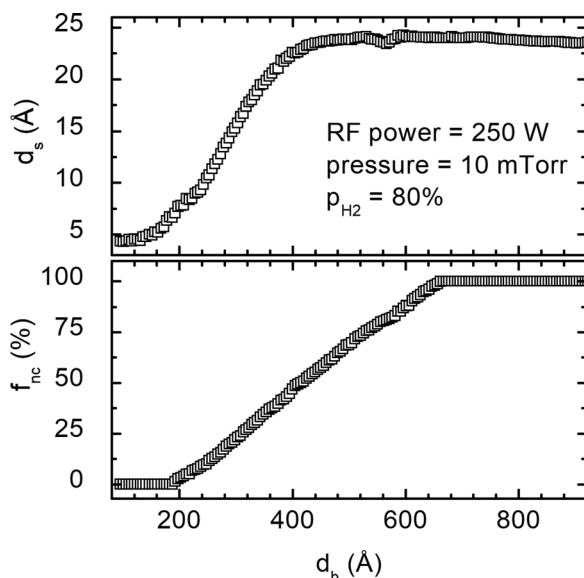


FIG. 4. Surface roughness and nanocrystallite fraction depth profile in the mixed-phase (a + nc) regime obtained from VIA of RTSE data for a high deposition rate film prepared at $p_{\text{H}_2} = 80\%$.

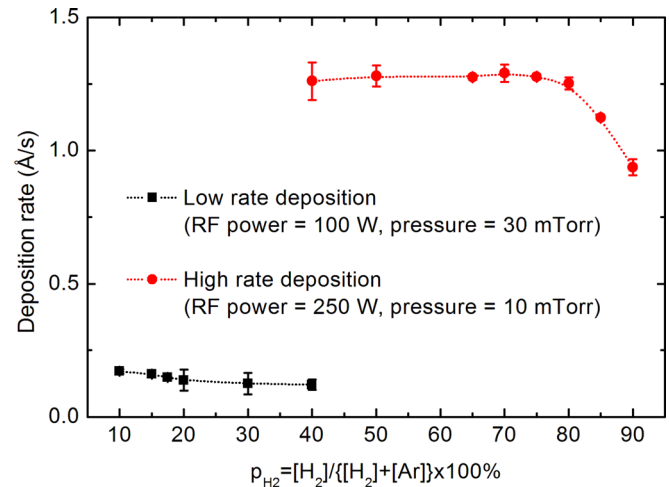


FIG. 5. Deposition rates as functions of p_{H_2} for low (black squares) and high (red circles) rate sputtered Si:H.

increasing the likelihood that the sputtered material is scattered away from the substrate by ambient Ar gas. By contrast, increases in RF power will increase the overall deposition rates mainly by increasing the flux of the material sputtered from the target. When RF power is increased and total pressure decreased simultaneously, these two effects result in the significantly increased deposition rate observed for the high rate film series. As is seen in Fig. 5, films with a RF power of 100 W and total pressure of 30 mTorr result in deposition rates ~ 0.15 Å/s compared to order of magnitude larger deposition rates of ~ 1.3 Å/s for films prepared with a RF power of 250 W and total pressure of 10 mTorr. For films remaining in the amorphous phase, the deposition rate is relatively stable for both low and high rate series. This rate remains stable for slightly higher p_{H_2} films that nucleate crystallites and evolve; however, further increases in p_{H_2} eventually result in a reduction in the growth rate. This reduction is seen in both series when crystallite nucleation occurs at <150 Å and coalescence at <400 Å. This behavior suggests that under higher p_{H_2} conditions, hydrogen may not be as effectively incorporated into the crystallites compared to a-Si:H and grain boundary material produced at relatively lower p_{H_2} . The lower deposition rate observed for high p_{H_2} after nanocrystallite coalescence may be due to etching of the weakly bound material on grain boundaries by additional unincorporated hydrogen. PECVD Si:H also shows a similar trend; however, decreasing growth rates are observed with increasing hydrogen dilution throughout the amorphous, mixed-phase, and nanocrystalline growth regimes.⁵

C. X-ray diffraction

Figure 6(a) shows the GIXRD patterns of films produced under high deposition rate conditions. Similar GIXRD patterns have been observed for low rate films (not shown). The (111) and (220) peaks of Si are observed at $2\theta \approx 28.4^\circ$ and 47.3° , respectively, for films with significant nanocrystallite fractions grown at higher values of p_{H_2} . As has already been demonstrated in the RTSE results, the films remain amorphous for lower p_{H_2} and nucleate nanocrystallites when p_{H_2} is $\geq 17.5\%$

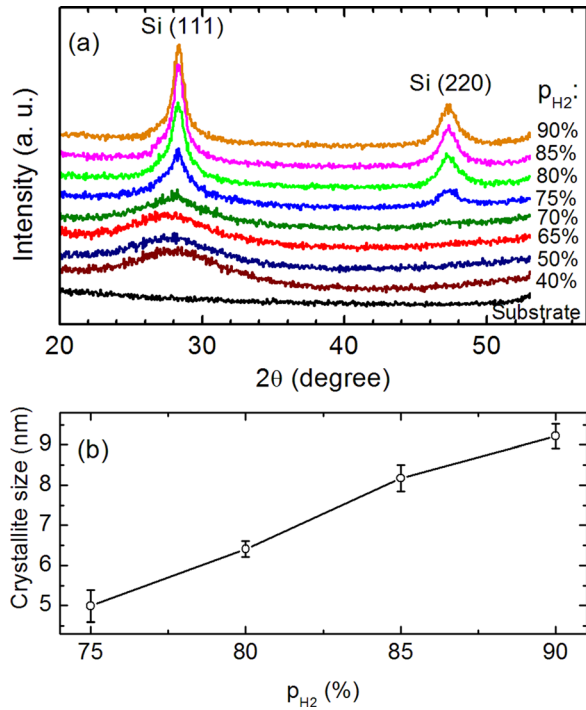


FIG. 6. (a) Grazing incidence x-ray diffraction (GIXRD) patterns of high deposition rate Si:H prepared at 250 W RF power and 10 mTorr total gas pressure with varying p_{H_2} as indicated. (b) Nanocrystallite grain size determined from GIXRD patterns as a function of p_{H_2} .

and $\geq 75\%$ for low and high rate films, respectively. The broad feature observed at about $2\theta \approx 28.4^\circ$ for high rate samples with $p_{H_2} \leq 70\%$ is similar to that reported for a-Si:H elsewhere.⁴⁴ The XRD peaks change from broad, low amplitude peaks (or none at all) to sharper, narrow peaks with increasing p_{H_2} , supporting the RTSE determined phase transformations depicted in Fig. 2(b). The significantly larger amplitude of the peak at 28.4° when compared to that at 47.3° indicates preferential crystallographic orientation along the (111) direction. The broadening of both diffraction peaks decreases and the amplitude increases with increasing p_{H_2} . This behavior indicates that the size and fraction of nanocrystallites increase with increasing hydrogen concentration during deposition. The crystallite size (d) has been obtained using Lorentzian fitting of (111) peaks and the Scherrer equation, given by⁴⁵

$$d = \frac{k\lambda}{\beta \cos \theta}, \quad (2)$$

where the shape factor $k = 0.9$, λ is the x-ray wavelength (in this case 1.54059 \AA for Cu_α), β is the diffraction peak full width half maximum, and θ is the angle of diffraction. Figure 6(b) shows the nanocrystallite grain size as a function of p_{H_2} for the higher deposition rate series of Si:H sputtered films. The grain size increases from 5.0 to 9.2 nm as p_{H_2} is increased from 75 to 90%, again indicating that increased hydrogen concentration in the sputter ambient is conducive to improved crystallinity. Previous studies on Si:H films prepared from RF sputtering,^{15,21} VHF-PECVD,²⁰ and PECVD^{11,44,46} observed similar XRD patterns with (111) preferential orientation and comparable nanocrystallite size as obtained here. Observations in the literature also show the

change of preferred orientation from (111) to (220) for different fabrication techniques including RF sputtered⁴⁷ and PECVD⁴⁶ materials depending on the deposition parameters.

D. Infrared optical properties

The electronic properties of both a-Si:H and nc-Si:H benefit from hydrogen passivation of defects associated with dangling bonds or grain boundaries.^{3,5,22} The transition strength of absorption features arising from silicon-hydrogen bonds provides a measure of the relative density of each bond type in the material. Several studies of the silicon-hydrogen (Si-H_n ; $n = 1, 2, 3$) bonding configurations' manifestation in IR vibrational modes are used as a guide in the fitting of the IR ellipsometric spectra and interpreting the results in this work.^{5,11,20-34} Three groups of vibrational modes corresponding to Si-H bonds are expected in Si:H, namely: stretching ($\omega^S = 2000, 2090, \text{ and } 2120 \text{ cm}^{-1}$), bending ($\omega^B = 850 \text{ and } 890 \text{ cm}^{-1}$), and wagging or rocking ($\omega^W = 640 \text{ and } \omega^R = 590 \text{ cm}^{-1}$). IR ellipsometric data are analyzed with a similar structural model to that used in RTSE data analysis with the IR absorption features in ϵ_2 parameterized by Gaussian oscillators⁴⁸ each expressed as:

$$\epsilon_2(E) = A e^{-\left(\frac{2\sqrt{\ln(2)}(E-E_n)}{\Gamma}\right)^2} - A e^{-\left(\frac{2\sqrt{\ln(2)}(E+E_n)}{\Gamma}\right)^2}, \quad (3)$$

where E_n , A , and Γ represent the resonance energy, amplitude, and broadening of each Gaussian oscillator, respectively. The real part, ϵ_1 , is obtained by a Kramers-Kronig integration of ϵ_2 given by⁴⁰

$$\epsilon_1 = \epsilon_\infty + \frac{2}{\pi} P \int_0^\infty \frac{\xi \epsilon_2(\xi)}{\xi^2 - E^2} d\xi, \quad (4)$$

where P is the Cauchy principal part of the integral and ϵ_∞ is a constant additive term to ϵ_1 . Among the possible expected IR-absorption modes, we have identified sensitivity to those centered at 590, 640, 2000, and 2090 cm^{-1} for this series of Si:H samples.

The Fourier transform IR measurements and the analysis are performed for both low and high deposition rate film series. Figure 7 shows an example of IR ϵ_2 spectra for $p_{H_2} = 50\%$ a-Si:H from the high rate series. The absorption feature centered at 590 cm^{-1} is attributed to the Si-H₂ rocking mode, that at 640 cm^{-1} is attributed to the Si-H_n ($n = 1, 2, 3$) wagging mode, and the modes at 2000 and 2090 cm^{-1} are attributed to Si-H and Si-H₂ stretching, respectively.²² For each of these features, the area under the peak can be used as a relative measure of the prevalence of the associated bond in the material.⁴⁹ The index of refraction, n , of all films (both low and high rate) at 5000 cm^{-1} , where Si:H is non-absorbing, is used to determine the relative density of each film compared to the densest material exhibiting the highest index of refraction, $n = 3.1979$, identified for Si:H produced at $p_{H_2} = 90\%$. Mass density calculated from this value is 2.15 g/cm^3 , indicating that these films may be considered moderately dense.^{26,27,50} The density of each film relative to the densest film at $p_{H_2} = 90\%$ is obtained by using $\epsilon = n^2$ at 5000 cm^{-1} and Equation (1) with $f_{mat} = 1 - f_{void}$. The low rate

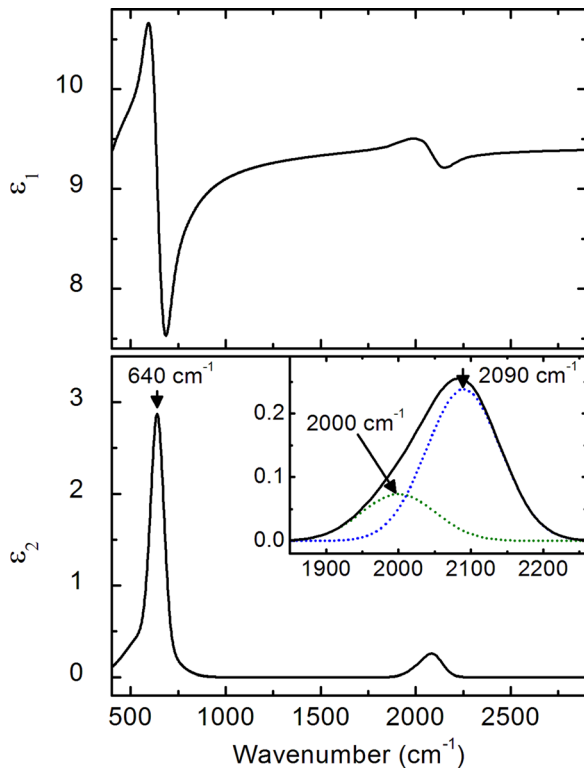


FIG. 7. Infrared (IR) spectra in ϵ , showing absorption features in ϵ_2 for a high deposition rate Si:H film produced at $p_{H_2} = 50\%$. The inset shows deconvoluted features at 2000 and 2090 cm^{-1} .

films are observed to have higher void fractions, lower material fraction, than high rate films relative to the densest film. This value of material fraction is used for the normalization of integrated area under the absorption peaks for both series of samples, and is shown in Fig. 8 for the high rate series. Normalization is performed to ensure that comparison of relative hydrogen incorporation from transition strengths of absorption features between films is not biased by variations in film density. Thus, the strength of the features related to silicon-hydrogen bonding in the optical response is not artificially dampened due to the presence of voids in low density materials decreasing the overall amplitude of spectra in ϵ .

Figure 8 shows the integrated area under the absorption peak as a function of p_{H_2} for each of the 640, 2000, and 2090 cm^{-1} peaks for the high rate film series. The absorption peak at 640 cm^{-1} is used to calculate the hydrogen content, C_H (at. %) in the film applying a similar procedure to that explained in Refs. 22 and 23 and the values are shown in Fig. 8 (top right vertical axis). The hydrogen content is also obtained for the low rate films. The value of C_H (at. %) seems to decrease at higher p_{H_2} for both series of samples, and it is observed that the higher rate samples have generally higher values of C_H (at. %) compared to low rate samples with C_H ranging from 2.6 to 6.7%. These values of hydrogen content seem reasonable in consideration of the values reported in Ref. 23. With increasing p_{H_2} in the high rate series, the area under each of the 640 and 2090 cm^{-1} absorption peaks first decreases then remains stable after the films become predominantly nanocrystalline at $p_{H_2} \geq 75\%$. The variations of the features at 2000 and 2090 cm^{-1} within the

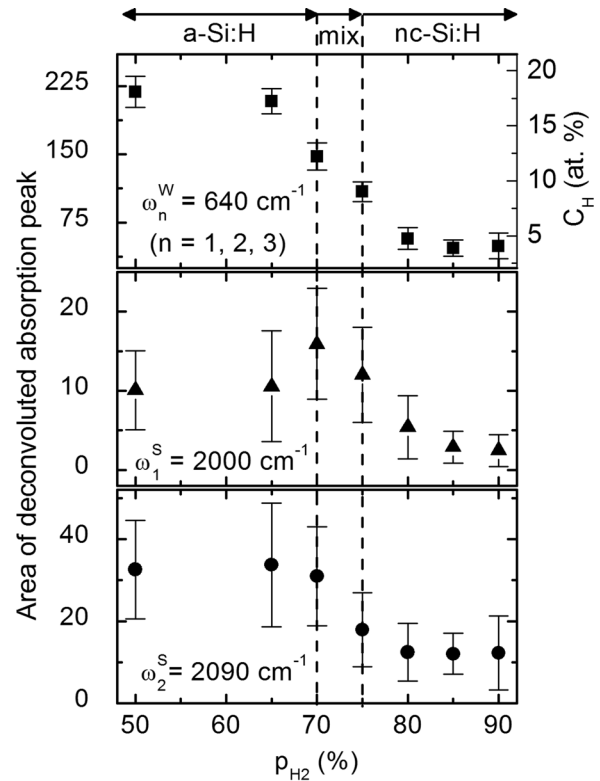


FIG. 8. Integrated areas under the absorption peaks centered at 640, 2000, and 2090 cm^{-1} as functions of p_{H_2} for the high deposition rate film series. The right vertical axis on the top panel represents H-content in the respective film and the dashed vertical transition lines identify the final phase reached for ~ 2500 Å thick samples.

a-Si:H regime for the high rate films are generally close to the error limits. The area under the 2000 cm^{-1} peak initially increases with increasing p_{H_2} , reaches a maximum at the maximum hydrogen concentration prior to any crystallite nucleation at $p_{H_2} = 70\%$, and then decreases quickly as nanocrystallites form in the film. Since the 2000 and 2090 cm^{-1} peaks are associated with monohydride (Si-H) and dihydride (Si-H₂) bonding configurations, respectively, these results suggest that monohydride bonding is more pronounced in a-Si:H and less so when the films become nanocrystalline.⁴¹

Similarly, for the low rate films, the area under each of the three peaks at 640, 2000, and 2090 cm^{-1} initially increases with increasing p_{H_2} , reaches a maximum at the maximum hydrogen concentration prior to or at which point crystallites starts to nucleate at $p_{H_2} = 17.5\%$, and then decreases quickly as the film becomes nanocrystalline. Also for the low rate films, a similar trend in which monohydride bonding, more pronounced in a-Si:H, is suppressed as the material becomes predominantly nc-Si:H. More importantly, the areas under all three peaks (640, 2000, and 2090 cm^{-1}) is significantly lower than the values for the corresponding peaks of high rate samples. Similarly, the relative density and hydrogen content for low rate films are lower than those for high rate films. All these observations indicate that the low rate Si:H is even more porous than the films in the high rate series and may lack sufficient hydrogen to passivate defects and dangling bonds.

Predominant Si-H₂ in a-Si:H is not desirable for solar cell absorber layer materials; however, both sets of films may still be suitable for grain boundary passivation in nc-Si:H layers or for passivation of crystalline silicon in wafer based devices. Significant features near 2100 cm⁻¹ arising from the grain boundary material in nc-Si:H layers are not necessarily linked to poor performance of a solar cell incorporating an intrinsic nc-Si:H absorber layer^{28,29,51} and are quite commonly reported in nc-Si:H films.⁵²⁻⁵⁴ Similarly, a porous^{55,56} and large amplitude high stretching mode features in the infrared spectrum^{1,57} of thin a-Si:H used as passivants for crystal silicon have also been observed. From the 640 cm⁻¹ peak in the films studied here, which is associated with all possible wagging modes Si-H_n (n = 1, 2, 3), the hydrogen content relative to the densest film decreases with increasing p_{H2}. This behavior may be due to the fact that grain size increases for higher p_{H2} films as observed from GIXRD and there is relatively less grain boundary surface area with fewer sites available for hydrogen incorporation. Previous studies of PECVD Si:H show that hydrogen incorporation increases with increasing hydrogen dilution within the amorphous growth regime. However, during mixed phase or nanocrystalline growth, hydrogen incorporation in the film decreases with increasing hydrogen dilution.^{41,47} The hydrogen content in the Si:H film depends strongly on the deposition parameters including temperature, pressure, and source gases.⁴¹

IV. CONCLUSIONS

The growth evolution of Si:H films produced via magnetron sputtering shows phase transformations from amorphous to mixed-phase then to single-phase nanocrystalline. In studies of the growth evolution diagrams, deposition rates are not observed to decrease at the lowest p_{H2} at which crystallites nucleate. As a result, similar growth rates are obtained between a-Si:H and nc-Si:H phases near what would be considered the protocrystalline region in PECVD Si:H. From IR spectroscopic ellipsometry measurements and analysis, Si-H_n bonding configurations have been identified with absorption peaks centered at 590, 640, 2000, and 2090 cm⁻¹. Samples with higher p_{H2} and lower deposition rates after crystallite coalescence exhibit lower relative amounts of hydrogen incorporation into the film, which may be due to the etching of weak Si-Si bonds on the growing surface by unincorporated reactive hydrogen.²¹ Overall, these results indicate that sputtering can be a useful deposition technique for producing nc-Si:H of reasonable quality as assessed by growth evolution diagrams at rates that are generally comparable to many CVD processes. Additionally, a-Si:H made by sputter deposition may serve as a potential candidate for passivation of crystalline Si without the need for silicon carrying source gases. Promising results have been obtained with similarly porous CVD a-Si:H in literature, therefore a challenge remains to see if similar material performance can be obtained with sputtered material.

ACKNOWLEDGMENTS

This work was supported by University of Toledo start-up funds, the Ohio Department of Development (ODOD)

Ohio Research Scholar Program (Northwest Ohio Innovators in Thin Film Photovoltaics, Grant No. TECH 09-025), and the Office of Naval Research (Grant No. 11847944).

- ¹H. Fujiwara and M. Kondo, *J. Appl. Phys.* **101**, 054516 (2007).
- ²M. Tanaka, M. Taguchi, T. Matsuyama, T. Sawada, S. Tsuda, S. Nakano, H. Hanafusa, and Y. Kuwano, *Jpn. J. Appl. Phys.* **31**, 3518 (1992).
- ³X. Deng and E. A. Schiff, *Handbook of Photovoltaic Science and Engineering*, edited by A. Luque and S. Hegedus (John Wiley & Sons, 2003), pp. 505-565.
- ⁴J. Yang and S. Guha, *Mater. Res. Soc. Symp. Proc.* **557**, 239 (1999).
- ⁵L. Karki Gautam, M. M. Junda, H. F. Haneef, R. W. Collins, and N. J. Podraza, *Materials* **9**, 128 (2016).
- ⁶R. W. Collins, A. S. Ferlauto, G. M. Ferreira, C. Chen, J. Koh, R. J. Koval, Y. Lee, J. M. Pearce, and C. R. Wronski, *Sol. Energy Mater. Sol. Cells* **78**, 143 (2003).
- ⁷J. M. Pearce, N. Podraza, R. W. Collins, M. M. Al-Jassim, K. M. Jones, J. Deng, and C. R. Wronski, *J. Appl. Phys.* **101**, 114301 (2007).
- ⁸J. Koh, Y. Lee, H. Fujiwara, C. R. Wronski, and R. W. Collins, *Appl. Phys. Lett.* **73**, 1526 (1998).
- ⁹A. S. Ferlauto, G. M. Ferreira, R. J. Koval, J. M. Pearce, C. R. Wronski, R. W. Collins, M. M. Al-Jassim, and K. M. Jones, *Thin Solid Films* **455-456**, 665 (2004).
- ¹⁰C. R. Wronski and R. W. Collins, *Sol. Energy* **77**, 877 (2004).
- ¹¹L. Xu, Z. P. Li, C. Wen, and W. Z. Shen, *J. Appl. Phys.* **110**, 064315 (2011).
- ¹²J. Koh, A. S. Ferlauto, P. I. Rovira, R. J. Koval, C. R. Wronski, and R. W. Collins, *J. Non-Cryst. Solids* **266-269**, 43 (2000).
- ¹³N. J. Podraza, C. R. Wronski, and R. W. Collins, *J. Non-Cryst. Solids* **352**, 950 (2006).
- ¹⁴T. D. Moustakas, in *Semiconductors and Semimetals*, edited by J. I. Pankove (Academic Press, N.Y., 1984), Vol. 21A, Ch. 4.
- ¹⁵P. Dutta, S. Paul, S. Tripathi, Y. Chen, S. Chatterjee, V. Bommisetty, D. Galipeau, and A. Liu, in *33rd IEEE Photovoltaic Specialists Conference* (2008), pp. 1-4.
- ¹⁶T. Tiedje, T. D. Moustakas, and J. M. Cebulka, *Phys. Rev. B* **23**, 5634 (1981).
- ¹⁷R. W. Collins, I. An, H. V. Nguyen, and T. Gu, *Thin Solid Films* **206**, 374 (1991).
- ¹⁸L. Houben, M. Luysberg, P. Hapke, R. Carius, F. Finger, and H. Wagner, *Philos. Mag. A* **77**, 1447 (1998).
- ¹⁹S. Muthmann, F. Köhler, M. Meier, M. Hülsbeck, R. Carius, and A. Gordijn, *Phys. Status Solidi RRL* **5**, 144 (2011).
- ²⁰D. Wang, Z. Yang, F. Li, and D. He, *Appl. Surf. Sci.* **257**, 8350 (2011).
- ²¹T. D. Moustakas, H. P. Maruska, and R. Friedman, *J. Appl. Phys.* **58**, 983 (1985).
- ²²M. H. Brodsky, M. Cardona, and J. J. Cuomo, *Phys. Rev. B* **16**, 3556 (1977).
- ²³A. A. Langford, M. L. Fleet, B. P. Nelson, W. A. Lanford, and N. Maley, *Phys. Rev. B* **45**, 13367 (1992).
- ²⁴E. C. Freeman and W. Paul, *Phys. Rev. B* **18**, 4288 (1978).
- ²⁵G. Lucovsky, R. J. Nemanich, and J. C. Knights, *Phys. Rev. B* **19**, 2064 (1979).
- ²⁶A. H. M. Smets, W. M. M. Kessels, and M. C. M. van de Sanden, *Appl. Phys. Lett.* **82**, 1547 (2003).
- ²⁷A. H. M. Smets and M. C. M. van de Sanden, *Phys. Rev. B* **76**, 073202 (2007).
- ²⁸A. H. M. Smets, T. Matsui, and M. Kondo, *J. Appl. Phys.* **104**, 034508 (2008).
- ²⁹A. H. M. Smets, T. Matsui, and M. Kondo, *Appl. Phys. Lett.* **92**, 033506 (2008).
- ³⁰M. Stuckelberger, M. Despeisse, G. Bugnon, J. W. Schütttauf, F. J. Haug, and C. Ballif, *J. Appl. Phys.* **114**, 154509 (2013).
- ³¹M. Stuckelberger, R. Biron, N. Wyrsh, F. J. Huang, and C. Ballif, *Renewable Sustainable Energy Rev.* **76**, 1497-1523 (2017).
- ³²J. Melskens, A. H. M. Smets, M. Schouten, S. W. H. Eijt, H. Schut, and M. Zeman, *IEEE J. Photovoltaics* **3**, 65 (2013).
- ³³J. Melskens, A. H. M. Smets, S. W. H. Eijt, H. Schut, E. Brück, and M. Zeman, *J. Non-Cryst. Solids* **358**, 2015 (2012).
- ³⁴J. Melskens, S. W. H. Eijt, M. Schouten, A. S. Vullers, A. Mannheim, H. Schut, B. Macco, M. Zeman, and A. H. M. Smets, *IEEE J. Photovoltaics* **7**, 421 (2017).
- ³⁵W. Paul and D. A. Anderson, *Sol. Energy Mater.* **5**, 229 (1981).

- ³⁶C. Chen, I. An, G. M. Ferreira, N. J. Podraza, J. A. Zapien, and R. W. Collins, *Thin Solid Films* **455–456**, 14 (2004).
- ³⁷B. Johs, J. A. Woollam, C. M. Herzinger, J. Hilfiker, R. Synowicki, and C. L. Bungay, *Proc. SPIE* **72**, 29 (1999).
- ³⁸H. Fujiwara, J. Koh, P. I. Rovira, and R. W. Collins, *Phys. Rev. B* **61**, 10832 (2000).
- ³⁹D. Adhikari, M. M. Junda, P. Uprety, K. Ghimire, I. Subedi, and N. J. Podraza, *Phys. Status Solidi B* **253**, 2066 (2016).
- ⁴⁰A. S. Ferlauto, G. M. Ferreira, J. M. Pearce, C. R. Wronski, and R. W. Collins, *J. Appl. Phys.* **92**, 2424 (2002).
- ⁴¹H. Fujiwara, M. Kondo, and A. Matsuda, *J. Appl. Phys.* **91**, 4181 (2002).
- ⁴²N. J. Podraza, J. Li, C. R. Wronski, E. C. Dickey, and R. W. Collins, *J. Vac. Sci. Technol., A* **27**, 1255 (2009).
- ⁴³Y. A. Kryukov, N. J. Podraza, R. W. Collins, and J. G. Amar, *Phys. Rev. B* **80**, 085403 (2009).
- ⁴⁴R. Amrani, P. Abboud, L. Chahed, and Y. Cuminal, *Cryst. Struct. Theory Appl.* **1**, 62 (2012).
- ⁴⁵P. Scherrer, *Nachrichten von der Gesellschaft der Wissenschaften zu Göttingen, Mathematisch-Physikalische Klasse* **2**, 98 (1918).
- ⁴⁶G. Ganguly, T. Ikeda, T. Nishimiya, K. Saitoh, M. Kondo, and A. Matsuda, *Appl. Phys. Lett.* **69**, 4224 (1996).
- ⁴⁷A. Achiq, R. Rizk, F. Gourbilleau, R. Madelon, B. Garrido, A. Pérez-Rodríguez, and J. R. Morante, *J. Appl. Phys.* **83**, 5797 (1998).
- ⁴⁸D. De Menezes, M. Malki, and P. Echegut, *J. Non-Cryst. Solids* **352**, 769 (2006).
- ⁴⁹H. Povolny, P. Agarwal, S. Han, and X. Deng, *Mater. Res. Soc. Symp. Proc.* **609**, A30.3.1-6 (2000).
- ⁵⁰Z. Remes, M. Vanecek, P. Torres, U. Kroll, A. H. Mahan, and R. S. Crandall, *J. Non-Cryst. Solids* **227–230**, 876 (2000).
- ⁵¹T. Sekimoto, M. Matsumoto, M. Hishida, and A. Terakawa, *Jpn. J. Appl. Phys.* **53**, 095501 (2014).
- ⁵²H. Fujiwara, Y. Toyoshima, M. Kondo, and A. Matsuda, *J. Non-Cryst. Solids* **266–269**, 38 (2000).
- ⁵³M. Cardona, *Phys. Status Solidi B* **118**, 463 (1983).
- ⁵⁴U. Kroll, J. Meier, A. Shah, S. Mikhailov, and J. Weber, *J. Appl. Phys.* **80**, 4971 (1996).
- ⁵⁵B. Macco, J. Melskens, N. J. Podraza, K. Arts, C. Pugh, O. Thomas, and W. M. M. Kessels, *J. Appl. Phys.* **122**, 035302 (2017).
- ⁵⁶W. Liu, L. Zhang, R. Chen, F. Meng, W. Guo, J. Bao, and Z. Liu, *J. Appl. Phys.* **120**, 175301 (2016).
- ⁵⁷H. Fujiwara and M. Kondo, *Appl. Phys. Lett.* **86**, 032112 (2005).